

A CMOS closed-loop miniaturized wireless power transfer system for brain implant applications

Nishat T. Tasneem¹ • Dipon K. Biswas¹ · Ifana Mahbub¹

Received: 4 February 2020/Revised: 25 August 2020/Accepted: 8 September 2020/Published online: 15 October 2020 © Springer Science+Business Media, LLC, part of Springer Nature 2020

Abstract

Near-field inductively coupled wireless power transfer (WPT) system has been extensively utilized for brain implant applications. Still, the efficient and reliable delivery of power is challenging as the received power varies due to different variabilities between the transmitter (TX) and the receiver (RX) coils. A closed-loop adaptive control system utilizing load shift keying, designed in the 0.5 μ m standard CMOS process for providing the required power to the implant load compensating for these discrepancies is proposed in this paper. Both the proposed TX and the RX coils are fabricated using FR4 substrate having the dimensions of 10×10 mm and 5×5 mm, respectively. By changing the supply voltage of the power amplifier, this adaptive closed-loop system regulates the transmitted power to deliver 5.83 mW of power to the load, which is the approximate mid-point of the threshold window. The system achieves power transfer efficiencies of 9% and 8% at 8 mm distance through the air and the tissue media, respectively. Preliminary results show that the miniaturized WPT module with the feedback-loop achieves 8% and 3% of efficiency improvement for 8 mm distance between the TX and the RX coils, compared to the open-loop counterparts.

Keywords Adaptive regulation · Brain implant · Load modulation · Threshold window · Wireless power transfer

1 Introduction

Recent progressions in near-field wireless power transfer (WPT) systems have a significant aspect for applications in implantable medical devices, i.e., optogenetic implants, retinal prosthetics, neural signal recording, deep brain stimulations, etc. [1–4]. This paper focuses on the design of a miniaturized WPT system for brain implant applications. Wirelessly powered brain implant allows avoiding bulky and bio-hazardous batteries and surgeries for replacement [5]. One of the critical aspects of the implantable WPT system is to maintain reliability by continuously providing the required power to the implant. A typical WPT system for an implant includes a receiver (RX) coil with subsequent blocks, i.e. rectifier, low-dropout regulator (LDO) or DC–DC voltage converter, and a load, which might be the sensor circuitry, or μ-light-emitting diode (μ-LED) for

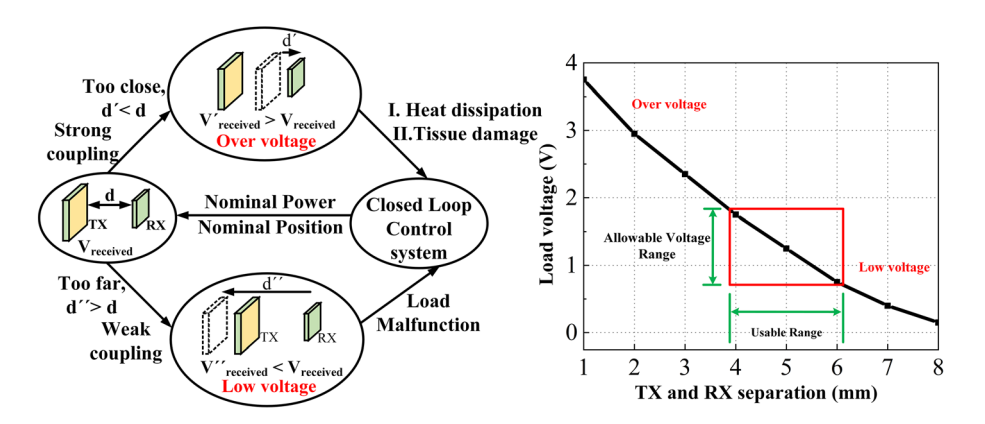
Different methods have been implemented to maximize the PTE of the WPT system: geometrical optimization, adaptive control of the delivered power, tuning of the operating frequency, etc. [8]. In order to ensure reliable and efficient operation of the implant, a regulation of the transmitting power is required to compensate for the constraints described above [9]. Without this control, there will be an excessive amount of transmitted power anticipating the worst-case scenarios (lowest coupling, highest load variation etc.), thus reducing the PTE of the system as shown in Fig. 1. Therefore, an adaptive control technique to regulate the transmitting power ensuring the continuous

optogenetic based neuromodulation application. Achieving a high-power transfer efficiency (PTE) of the system is a challenge as the received power varies due to various constraints. For instance, loose-coupling due to environmental variabilities namely co-axial or lateral displacements, angular misalignment due to the orientation of the inductive link pair, frequency mismatches between the (transmitter) TX and the RX coils, and the variation of the load impedance can degrade the PTE [6, 7].

Nishat T. Tasneem nishattarannumtasneem@my.unt.edu

Department of Electrical Engineering, University of North Texas, Denton, TX 76207-7102, USA

Fig. 1 Effects of displacement between TX and RX



and constant delivery of the power to the implant is imperative [10, 11].

Several schemes have been proposed for the adaptive control of the wireless power transmission in the literature. Back telemetry scheme using load shift keying (LSK) technique is implemented for efficient transmission of the power [12]. For realizing back telemetry, received power information at the receiver side is sent wirelessly to the transmitter side to regulate the transmitted power accordingly. Traditionally back telemetry is used to send this data over the same link [6, 9, 12, 13]. In these works, the regulation circuitry for controlling the system utilized additional physical components that increased the total implant size and weight [14], thus making the system complicated and unsuitable for brain implant applications. Most of the previously proposed designs include MCUs, commercialoff-the-shelf components (COTS), and field-programmable gate array (FPGA) implementations that make the implanted device too bulky and require more power from the primary side to be transmitted [15, 16]. Applicationspecific integrated circuit (ASIC) implementation of the required components to realize the back-telemetry system can be designed to resolve the aforementioned problems [9]. By combining both the CMOS process and the FPGAs, different losses due to various loading and coupling change effects are compensated in the system proposed by Huang et al. [9]. In this work, additional signal processing circuitry and analog-to-digital converter (ADC) are needed to implement the proposed power regulation system, thus making it power-hungry and degrading the overall PTE.

Most of the LDOs operate for a range of input voltages to provide a constant output voltage to the load. Previously proposed closed-loop WPT systems only had a single threshold voltage, where the rectified output voltage is compared with that threshold voltage. Then the transmitted power is either increased or decreased accordingly. This phenomenon causes an increase in the switching frequency of the controller loop whenever the load voltage goes below or exceeds the threshold voltage, eventually

increasing the average power consumption. A WPT system focusing on the regulation of the transmitted power within the working range of the preceding LDO is presented in this paper. This scheme allows the switching for implementing LSK only when the delivered power is above or below the working range. In our prior work, only the proposed feedback-loop scheme overview and simulation results were presented [10], while in this paper, the experimental validation of the closed-loop system with an actual miniaturized WPT module is presented along with the detailed description of the individual blocks.

The contributions of this paper are summarized as follows: the design of a miniaturized closed-loop WPT system for brain implant application is presented with detailed block-level description. The proposed feedback-loop can adaptively regulate the transmitting power within a certain range using a hysteresis comparator, compensating the various losses in the received power. The closed-loop is realized in ASIC implementation to utilize the back-telemetry approach through the LSK technique. An overview of the proposed closed-loop system is presented in Sect. 2, followed by the simulation and measurement results in Sect. 3. A concluding remark is then provided in Sect. 4.

2 Overview of the closed-loop wireless power transfer system

An overview of the proposed WPT system with load modulation scheme is shown in Fig. 2. It consists of three main blocks: the transmitter–receiver (TX–RX) block, an adaptive control unit (ACU) and a load section. The TX–RX block has a pair of inductively coupled coils L_1 – L_2 , two corresponding resonating capacitors C_{tx} – C_{rx} , and a class-E power amplifier (PA) to drive the transmitter coil. The load section of the system includes a voltage-doubler as the full-wave rectifier, a Schmitt-trigger based hysteresis comparator, a positive and a negative edge detector and



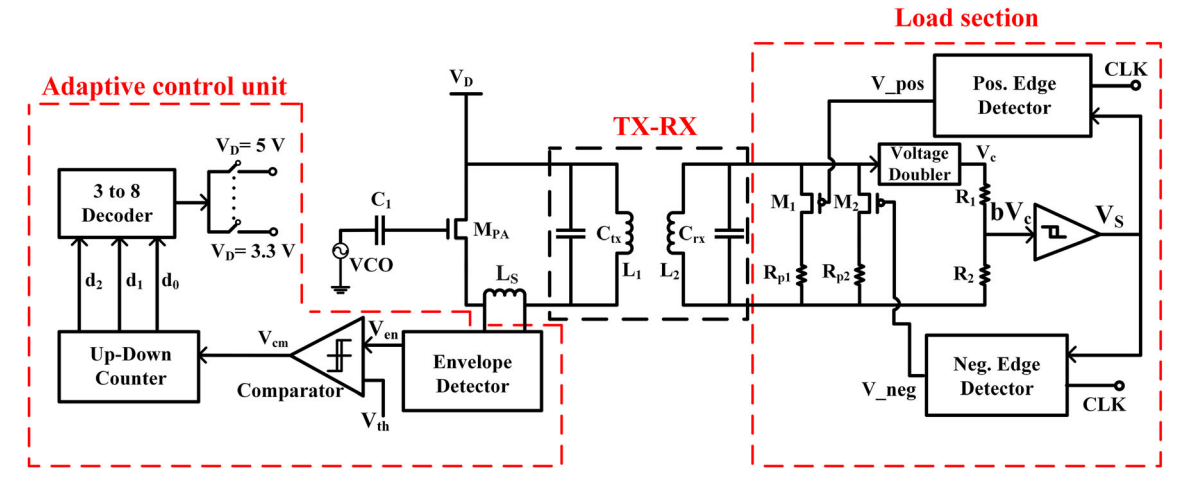


Fig. 2 Overview of the proposed adaptive closed-loop wireless power transfer system

two pMOS switches (M_1-M_2) to enable the load modulation method. Depending on the received power, there are two different load impedances R_{p1} and R_{p2} connected in series with the switches to modulate the reflected impedance seen from the primary side. A current sensing inductor L_s senses the primary current change due to the load impedance variations on the secondary side. An envelope detector then detects the voltage change across L_s . This change in the magnitude of the voltage is processed in the ACU which includes a static comparator and an asynchronous 3-bit up-down counter. A 3-to-8 bit decoder is also included to choose from one of the eight supply voltages of the PA depending on the output bits of the 3-bit counter.

The proposed WPT module is designed to resonate at 13.56 MHz by choosing the resonating capacitors C_{tx} and C_{rx} accordingly. The details of the TX and the RX coils design are discussed in the next subsection. A low frequency has been chosen in this paper, but the system can be validated for other high-frequency applications as well. The transmitter side includes a highly efficient (90–95%) class-E power amplifier [17]. The W/L or the aspect ratio of the power amplifier transistor (M_{PA}) has been chosen as 20 μm/0.6 μm. The length is kept as the minimum attainable channel length for the given process (0.5 µm CMOS) to reduce the drain resistance [18]. The transistor is biased in such a way to be operating in the triode region. A voltage-controlled oscillator (VCO) provides 13.56 MHz RF signal to the input of M_{PA} . The capacitor C_1 blocks the DC component of the VCO signal.

The flowchart of the adaptive control of the WPT system is shown in Fig. 3. It shows the algorithm to maintain the load voltage within a certain range considering the variations in the link efficiency. The transmitting resonating coil L_1 is driven by the PA and the flux generated by the TX coil results in a secondary voltage induced to L_2 . A full-

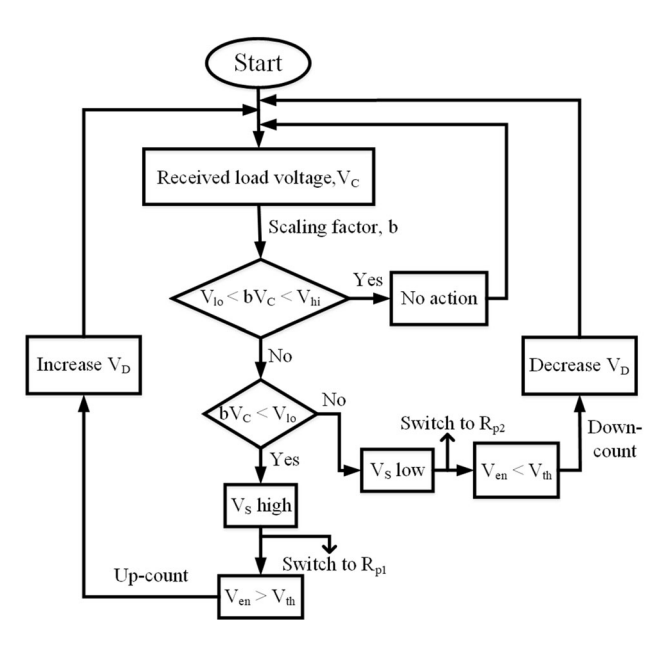


Fig. 3 Flow-chart of the adaptive control algorithm

wave rectifier rectifies the induced AC signal. The rectified DC voltage (V_c) is then supplied to the load. This load voltage varies with any variation in the coupling between the TX-RX coils due to the displacement or misalignment between them. V_c is scaled down to bV_c to keep it within the working range of the following Schmitt trigger as shown in (1).

$$bV_c = \frac{R_2}{R_1 + R_2} V_c \tag{1}$$

The values of the voltage divider circuitry R_1 and R_2 are chosen as 1 k Ω and 4.5 k Ω respectively to set the value of b as 0.8. The Schmitt trigger can detect any mismatch in bV_c , if it goes beyond the threshold window of it. The upper and the lower thresholds of the Schmitt trigger are designed to be 1.4 V and 0.676 V respectively to meet the



designated range. When the scaled voltage bV_c decreases lower than the lower boundary of the threshold window, the Schmitt trigger output V_s goes high and can be detected by the positive edge detector circuit (Fig. 2). The pMOS switch M_1 is turned on by the output of the positive edge detector (V_{pos}) , and the effective load impedance becomes R_{p1} . The vice versa happens when bV_c goes higher than the upper boundary of the Schmitt trigger window. V_{neg} from the negative edge detector turns on the M_2 switch changing the load impedance as R_{n2} . To differentiate the variation in the load impedances, the values of R_{p1} and R_{p2} are chosen as 5 k Ω and 10 k Ω respectively. As the load impedance varies due to the change in the load voltage, the current through the RX coil varies accordingly. The two currents for the two load impedances affect the primary (TX) current as well and can be sensed by detecting the voltage across the current sensing inductor L_S in the TX side. The envelope of the sensed voltage, V_L across the inductor due to the primary current change is detected by the envelope detector circuitry as shown in (2).

$$V_L = L \frac{di_p}{dt} \tag{2}$$

The envelope detector is a diode-based rectifier circuit that converts the AC voltage V_L to a DC voltage V_{en} , and then V_{en} is compared to a threshold voltage (V_{th}) of 0.6 V with the help of a static comparator. The output voltage of the comparator V_{cm} enables up-counting of the asynchronous 3-bit up-down counter, if it is greater than V_{th} . Based on the 3-bit output from the counter that increments every clock cycle till $V_{en} \leq V_{th}$, the 3-to-8 bit decoder keeps increasing the V_D of the PA from 3.3 to 5 V with an increment of 0.3 V. The eight different voltage levels are realized by using resistive divider circuit for each of the output of the decoder. In order to reduce the power consumption associated with the resistors, diode-connected nMOS transistors are used. They are designed in such a way to operate in the triode region. Since these resistive dividers are in the transmitter block, the voltages are coming from a voltage regulator. The additional overhead of the control block would be the voltage regulator overhead, which is connected to a battery. As the TX power proportionately varies with the PA supply voltage, changing V_D regulates the transmitted power to provide the required voltage V_c to the load. The detailed description of these blocks is provided in the following subsections.

2.1 Transmitter and receiver coil characterization

The TX-RX block of the WPT module is designed and modeled using Ansys HFSS (High-Frequency Structure Simulator) software. In our prior work, the TX-RX coils

were designed to model the path loss and PTE through air and brain tissue media [19]. The effects on PTE due to different combinations of displacements such as coaxiallateral and coaxial-angular misalignments were also presented. This work validates the closed-loop system integrated circuit with the proposed WPT system as a model to deliver continuous and regulated power to the load compensating for these variabilities. In order to optimize the performance of the WPT module, the inductance (L) and the quality factor (Q) of the TX and the RX coils and the mutual inductance (M_{12}) between them would need to be improved [20]. The RX coil used for the proposed closedloop system is a square-shaped spiral coil [21]. Both the TX and the RX coils are modeled using copper conductor on the FR4 substrate. The RX coil has 6 turns with trace width and trace spacing of 0.2 mm. The total dimension of the RX coil is 5×5 mm. The dimension of the TX spiral coil is 10×10 mm which has 2 turns with 0.5 mm trace width. Both the TX and RX coils are modeled using Ansys HFSS and and are shown in Fig. 4 with detailed dimensions. The fabricated antennas are shown in Fig. 5. The TX and RX coils are fabricated to resonate at 13.56 MHz frequency which is within the industrial, scientific, and medical radio (ISM) band. The Q-factors for the TX and the RX coils are measured as 52 and 28.2, respectively at 13.56 MHz. To resonate the RX coil at 13.56 MHz, a resonating capacitor of 1 nF is used in parallel to the coil. Similarly, a 2.2 nF capacitor is used to resonate the TX coil at the same frequency. The simulated and measured return losses of the RX coil are presented in Fig. 6. At the resonating frequency, the measured return loss of the RX coil is found to be -5.41 dB. The simulated and measured return losses of the TX coil are - 16.46 dB and - 16.05 dB respectively as shown in Fig. 7. The coil dimensions and other measured parameters for the TX and RX coils are listed in Table 1.

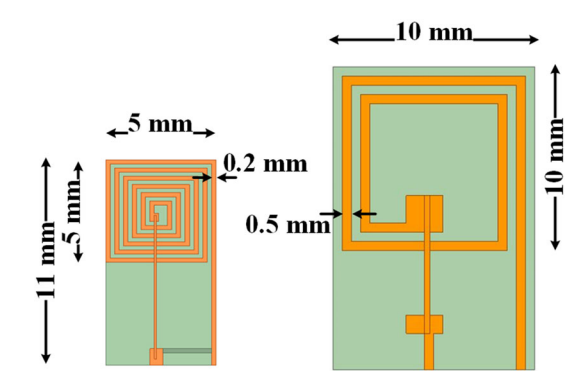


Fig. 4 Modeled TX and RX coils in HFSS





Fig. 5 Fabricated TX and RX coils

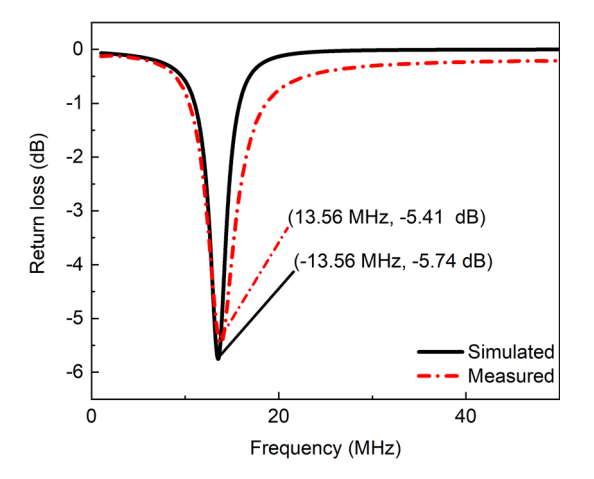


Fig. 6 The return loss of the RX coil

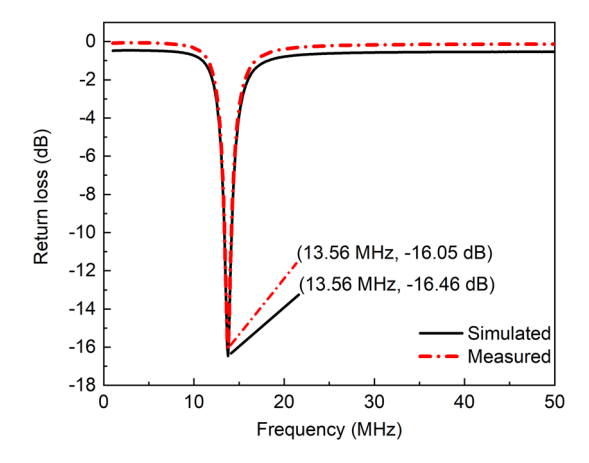


Fig. 7 The return loss of the TX coil

2.2 Load section

2.2.1 Voltage-doubler and Schmitt trigger

Figure 8a shows the voltage-doubler based full-wave rectifier to rectify the received AC signal at the load section side [22]. The rectifier uses Schottky diodes for the low forward bias voltage requirement ($\sim 150 \text{ mV}$) compared to the p-n junction diodes. In the negative half-cycle of the input ac signal, diode D_1 is forward-biased and C_1 is

Table 1 Coil dimensions and other measured parameters

	TX coil	RX coil
Size (mm ²)	10 × 10	5 × 5
Width (mm)	0.5	0.2
Spacing (mm)	0.5	0.2
Number of turns	2	6
Operating Frequency (MHz)	13.56	13.56
Q-factor	52	28.2
Inductance (nH)	69.88	91.17
Return loss (dB)	- 16.05	- 5.41
Resonating capacitance (nF)	2.2	1

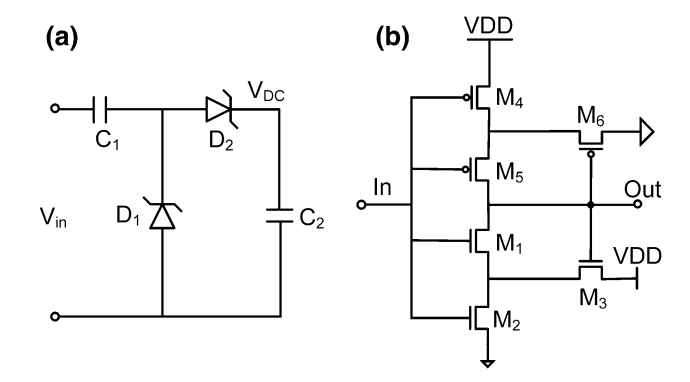


Fig. 8 Schematics of the a voltage-doubler, b Schmitt trigger

charged to V_m -the amplitude of V_{AC} . In the positive halfcycle, C_2 is charged to $2V_m$, as D_2 is positive-biased and D_1 is reverse-biased, and the charge in C_1 cannot discharge through D_1 . Thus, V_C becomes the dc voltage of $2V_m$. The values of both the capacitors C_1 and C_2 are chosen as 100 pF to provide a smooth DC output voltage, V_c . bV_c is compared with the two threshold voltages (V_{lo} and V_{hi}) of the Schmitt trigger for regulating the delivered power to the load within the threshold range. The schematic of the designed Schmitt trigger is shown in Fig. 8b. When the bV_c is lower than V_{lo} , M_4 and M_5 turn on and this provides the output signal a DC path to VDD. Transistors M_1 and M_2 turn on when bV_c goes higher than V_{hi} , providing the output a path to ground. The transistors are sized accordingly to get the upper and lower threshold voltages of 1.4 V and 0.676 V respectively, which corresponds to the V_c range of 1.75–0.75 V. The positive and negative edge detectors after the Schmitt trigger are implemented using the basic D-flipflop circuit [23].



2.3 Adaptive control unit

2.3.1 Envelope detector and static comparator

A simplified rectifier-based envelope detector is designed to detect the changes in the primary current through the current-sensing inductor (L_s) . The schematic of the envelope detector circuit is shown in Fig. 9. The capacitor C stores the charge from the incoming signal on the positive edge and discharges slowly through the resistor R. The value of C and R are chosen as 2 pF and 10 k Ω , respectively. A Schottky diode-based approach is considered in the design due to its low forward voltage drop compared to the traditional p-n junction-based diode. The envelope voltage of $V_L(V_{en})$, which is the DC voltage output of the envelope detector is compared with V_{th} using a comparator as shown in Fig. 10. If V_{en} is greater than the reference voltage (V_{th}) , the output (V_{out}) gives a high signal. If it goes lower than V_{th} (V_{ref} in Fig. 10), V_{out} goes low. M_{14} and M_{15} are working as the current sources to provide the bias current to M_{11} , M_{12} , and $M_{13} \cdot M_1$ and M_2 are the input transistors of the comparator. V_{th} is chosen as 0.6 V based on the corresponding primary current change when the load is switched from the regular load impedance to R_{p1} . The up-down counter and the 3-to-8-bit decoder at the transmitter side are designed using the D-flipflops [24].

3 Closed-loop system modeling

An analytical modeling of the closed-loop wireless power transfer is conducted for the stability analysis of the system. Since this work focuses on the regulation of the transmitted power compensating for the variation in the load voltage change, the adaptive control threshold is set as the input to the feedback system as shown in Fig. 11. The system is divided into three blocks as discussed earlier. The modeled forward path is consisted of the control unit at the transmitter, the PA and the inductive link, and the rectifier with capacitive-resistive $(C_L - R_L)$ load. The feedback path includes the load modulation circuit with adaptive thresholding. The control unit regulates the PA supply voltage according to the feedback path data during load

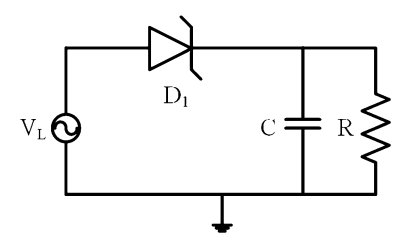


Fig. 9 Schematic of the envelope detector



modulation. The back-telemetry acts like an adder to either increase or decrease the PA supply to control the transmitted power. It can be represented as an integrator, following the transfer function in *z*-domain as shown below:

$$\frac{Y(z)}{X(z)} = \frac{k_I}{1 - z^{-1}} \tag{3}$$

where k_I is the DC gain of the control unit, Y(z) is the output which is fed to the next block as the supply voltage of the PA. X(z) is the input which is the load modulated back telemetry data, which is also the voltage across the sensing inductor L_s . The inductive link can be modeled as only a gain factor k_{ind} , which is the link efficiency. The rectifier output voltage V_c provides the load current through the R_L and C_L branch. When V_c goes beyond the Schmitt trigger window turning on either the R_p or $2R_p$, the total impedance of the receiver becomes as follow:

$$G(z) = \frac{V_c(z)}{I(z)} = \frac{R_L}{1 + \frac{R_L C}{T} + \frac{R_L}{2R_p} - \left(\frac{R_L C}{T} + \frac{R_L}{2R_p}\right)z^{-1}}$$
(4)

where T is the counter clock period, that is also the clock period of the positive and negative edge detector. The full closed-loop transfer function in the *z*-domain of the system then becomes:

$$\frac{V_{th}}{V_c} = \frac{k_{ind}k_IR_L}{\left(\frac{R_LC}{T} + \frac{R_L}{2R_p}\right)z^{-2} - \left(\frac{2R_LC}{T} + \frac{2R_L}{2R_p}\right)z^{-1} + k_{ind}k_IR_L + 1 + \left(\frac{R_LC}{T} + \frac{R_L}{2R_p}\right)}$$
(5)

where V_{th} (reference voltage of the comparator) is the input of the closed-loop system. The system's two poles can be expressed as:

$$Z_{1,2} = \frac{\left(\frac{2R_LC}{T} + \frac{2R_L}{2R_p}\right) + 1 \pm \sqrt{1 - \left(\frac{4R_L^2C}{T} + \frac{2R_L^2}{R_p}\right)k_Ek_I}}{2\left(k_Ek_IR_L + \frac{R_LC}{T} + \frac{R_L}{2R_p} + 1\right)}$$
(6)

The system is stable if and only if the magnitude of the transfer function in Eq. (5) is less than one. It can be shown that the two poles reside within the unit circle, resulting in the magnitude being less than one and the system being stable.

4 Simulation and measurement results

The proposed closed-loop control of the WPT system is designed in the 0.5 μm standard CMOS process. Any mismatch such as the displacement and angular misalignment between the TX and the RX coils degrade the link efficiency of the WPT system resulting in an inefficient operation of the implant. The information regarding the variation of the load voltage is thus necessary to regulate

Fig. 10 Schematic of the static comparator

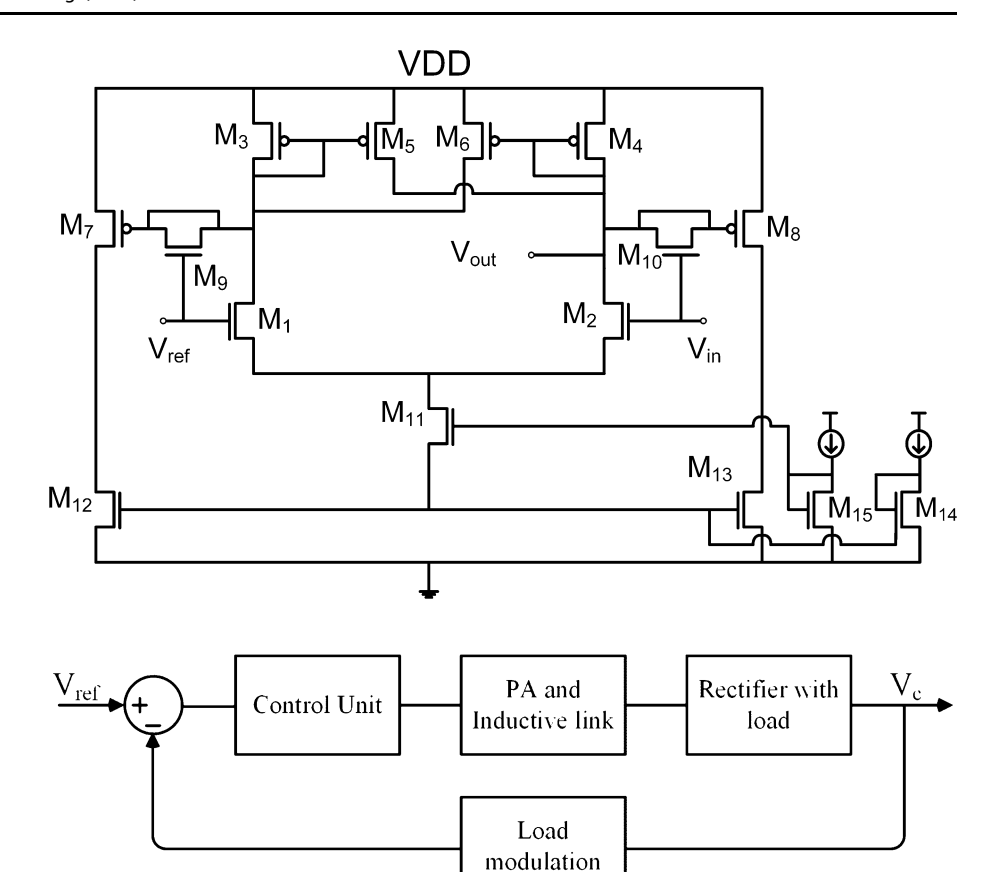


Fig. 11 Closed-loop modeling with load modulation as the back telemetry

the transmitted power to compensate for the variabilities accordingly.

As the scaled-down load voltage bV_c exceeds or falls below the Schmitt trigger threshold window, the output of the Schmitt trigger, V_s becomes low (0 V) or high (3.3 V) respectively. When bV_c is within the window, V_s doesn't have any effect. Figure 12 shows three different case scenarios (load voltage within and beyond the threshold window). The negative or the positive edge detector can

detect the shift in V_s value (low or high) and turns on the switches M_2 and M_1 respectively, as shown in Fig. 12. As the load is modulated by the switching between R_{p1} and R_{p2} , there are corresponding changes in the secondary current (di_s/dt) . Primary side current (di_p/dt) also increases or decreases proportionally to (di_s/dt) , due to the mutual coupling between the TX and the RX coils. The envelope detector detects the induced voltage in L_s because of the change in the primary coil current. Figure 13 shows the three case scenarios. The up–down counter counts either up

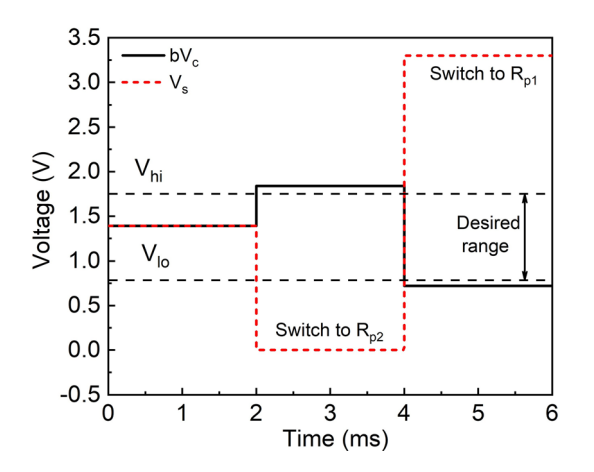


Fig. 12 Measured load voltage and Schmitt trigger output for varying distance

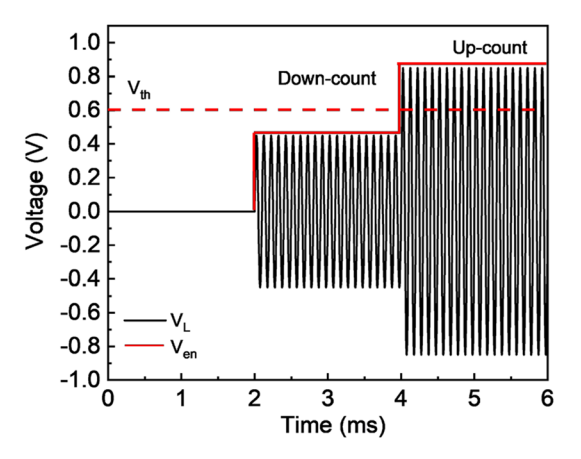


Fig. 13 Measured adaptive control unit outputs



or down based on the mechanism described in the previous section. Thus, the next higher or lower level of V_D is enabled to regulate the transmitting power.

The overall efficiency of the WPT module is calculated as follows:

$$\eta\% = \eta_1\% \times \eta_2\% \tag{7}$$

where η_1 is the inductive-link power transfer efficiency and η_2 is the voltage conversion efficiency (VCE) of the voltage-doubler based rectifier. Figure 14 shows the voltage conversion efficiency of the voltage-doubler in the load section. Voltage-doubler converts the received AC power to DC and approximately doubles the magnitude as well. As can be seen from Fig. 14, the higher the input AC voltage magnitude, the higher the rectifier DC voltage. Figure 14 shows the VCE of the rectifier for the range of load voltages of 0.75-1.75 V. The corresponding power conversion efficiency (PCE) is 41.7% for the above range. In order to regulate the load voltage within the range, the received power is aimed to be within 4-8 mW. All the simulation and measurement results for the closed-loop system presented in Figs. 15 and 14 show the data points when the received power is ~ 5.8 mW, which is the approximate mid-point of this range. The measured received power for the WPT system without any power regulation for varying the distance is shown in Fig. 13a, keeping the transmitted power at a constant value of 64.7 mW. The received power varies from 9.78 to 1.27 mW for varying the coaxial distance between the TX and the RX coils. The corresponding PTEs are presented in Fig. 16a. Figure 15b shows the regulated transmitted power to maintain the received power to ~ 5.83 mW. The transmitted power changes from 26.5 to 64.7 mW for compensating the variation in the mutual coupling between the coils due to the variations in coaxial distance. The aforementioned graphs indicate an overall PTE improvement in the closed-loop system compared to the open-loop

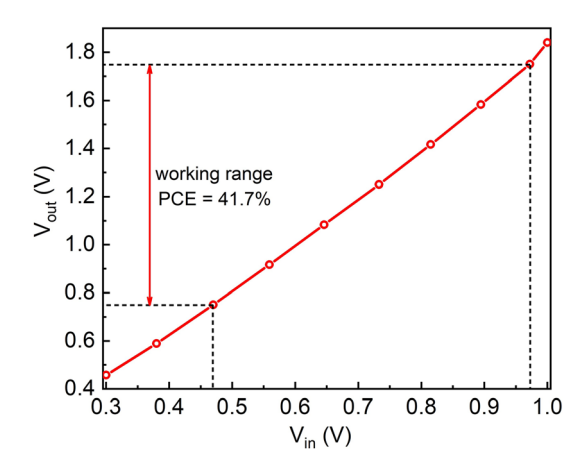


Fig. 14 Voltage conversion efficiency of the voltage-doubler



counterpart. At closer distances, the transmitted power is less than the open-loop transmitted power. Figure 16a, b shows the measured PTE through the air and the chicken breast as tissue media, respectively. To characterize the suitability of the closed-loop WPT system for implant applications, chicken breast is used in the measurement. In the open-loop system, the transmitted power is kept constant to provide the required power even at the worst-case misalignment condition, which is the 8 mm separating distance between the TX and the RX coils. The open-loop efficiency thus degrades over the distance, having higher received power than needed at closer distances, causing tissue damage. The biological tissue damage occurs from the consequences of the radiation from high heat dissipation. To emulate the tissue media in measurement set-up, chicken breast with different thicknesses are used. The system achieves 22% efficiency at 2 mm distance through the air media, while it achieves 16.6% efficiency through the chicken breast as the tissue media. Even at the farthest separation, the PTE of the closed-loop system compared to the open-loop system is improved by 8% and 3% respectively, and provides the required power of ~ 6 mW.

The total power consumption with the proposed closedloop control system is 2.9 mW for the load section with 3.3 V supply voltage, whereas the ACU consumes 13 mW excluding the PA power consumption, which is a function of the supply voltage. The test setup through the tissue and microphotograph of the chip are shown in Fig. 17a, b respectively. A comparison of the proposed system with the previously published works is presented in Table 2. As can be seen from the table, other works mostly used COTS and bulky components such as FPGA for achieving a high efficiency, while this paper presents only the ASIC implementation with 22% and 16.6% efficiency through air and the tissue media, respectively for the near-field coupling condition. It achieves an improvement in efficiency of 8% and 3% compared to the open-loop counterpart at the worst-case misalignment condition (8 mm distance). The paper also presents a miniaturized WPT system, which is compatible for brain implant application with such low power consumption.

5 Conclusions

A closed-loop power regulation system-on-a-chip is designed for brain implant applications such as optogenetic neuromodulation that can adaptively regulate the transmitted power based on the decision from the load modulation at the receiver side. Whenever the load voltage goes beyond the threshold window of a certain range, the load section and the adaptive control unit modulate the transmitted power instantaneously without the need for power-

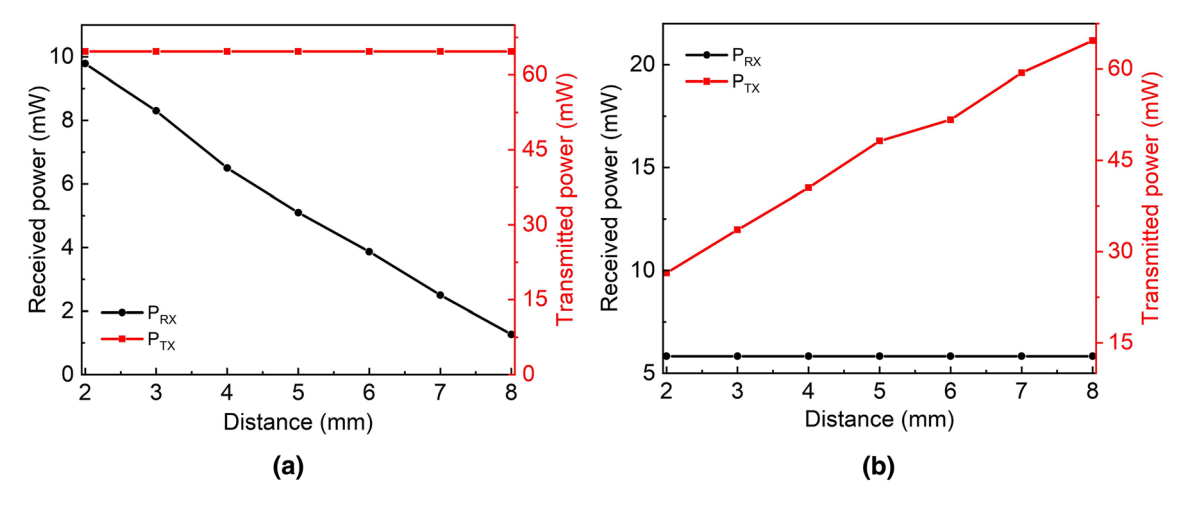


Fig. 15 a Received power for open-loop and b transmitted power for closed-loop system over distance

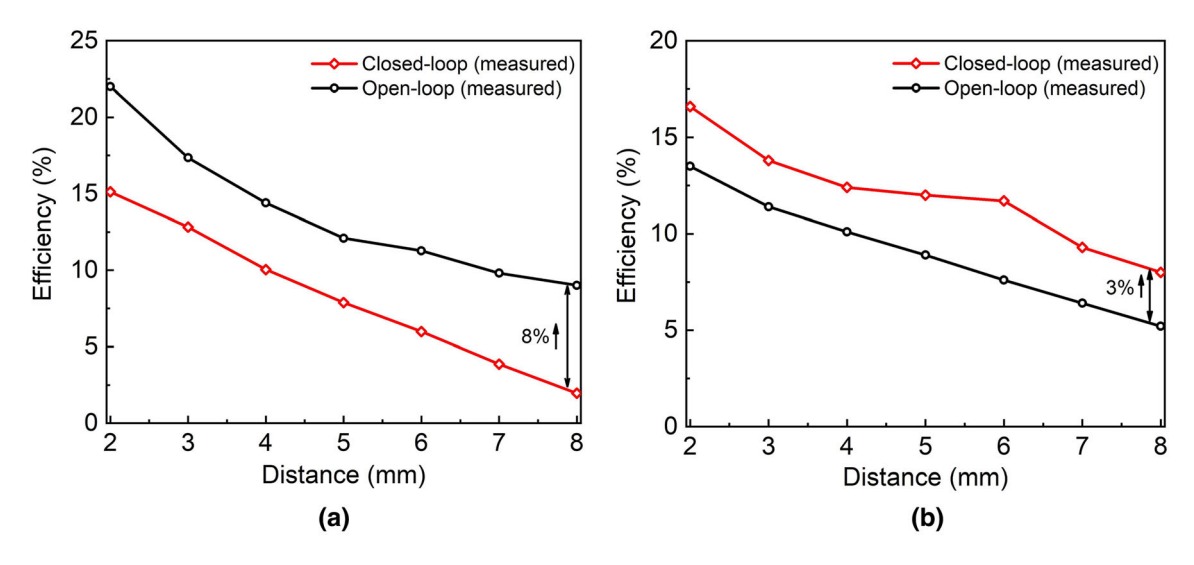


Fig. 16 Efficiency over displacement between TX and RX \boldsymbol{a} through air, \boldsymbol{b} through tissue

Fig. 17 a Test bench setup for measurement, b chip microphotograph of the ACU and load section

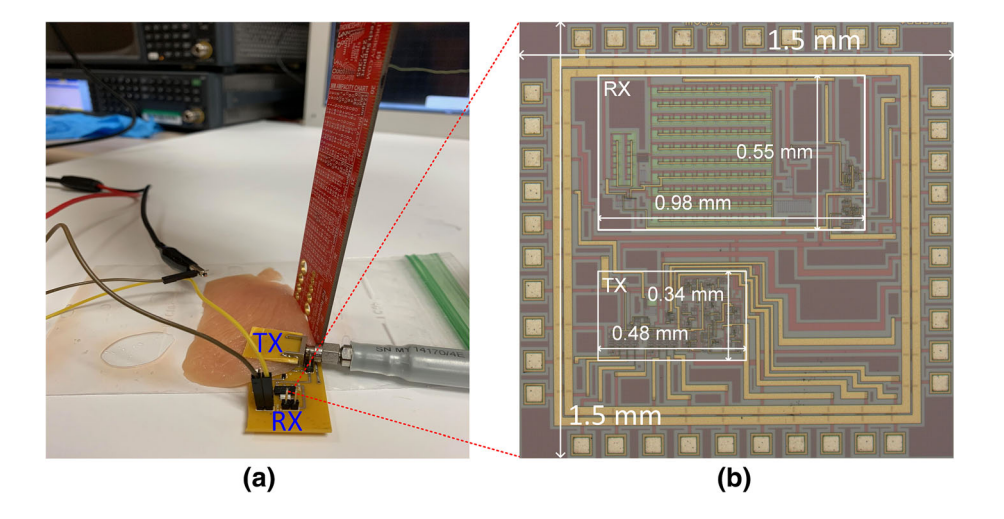




Table 2 Comparison with other works

	[8]	[12]	[15]	This work
Carrier frequency (MHz)	13.56	nr	13.56	13.56
Coil configuration	3 coils	2 coils	2 coils	2 coils
TX coil dimension	28 mm (C)	40 mm (C)	20 mm(C)	10 mm (S)
TX inductance	361 nH	69 μΗ	0.4 μΗ	70 nH
RX coil dimension	34 mm (C)	22 mm (C)	10 mm (C)	5 mm (S)
RX inductance	729 nH	60 μΗ	0.48 μΗ	91.2 nH
Implementation	COTS	ASIC, FPGA	COTS	ASIC
Efficiency	13.5%	33.3%	6.9%	22, 16.6%
TX/RX communication	LSK	LSK	LSK	LSK
Power consumption	$224~\mu W$	nr	10 mW	Load section: 2.3 mW
				ACU: 79.6 mW
				(including PA transmitted power)

hungry blocks. This closed-loop feedback system based on the hysteresis comparator allows transmitting the required power for a reliable operation of brain implant.

Acknowledgements This work is based upon work supported by the National Science Foundation (NSF) under Grant No. ECCS 1943990.

References

- Yeh, A. J., Ho, J. S., Tanabe, Y., Neofytou, E., Beygui, R. E., & Poon, A. S. (2013). Wirelessly powering miniature implants for optogenetic stimulation. *Applied Physics Letters*, 103(16), 163701.
- Akin, T., Najafi, K., & Bradley, R. M. (1998). A wireless implantable multi-channel digital neural recording system for a micromachined sieve electrode. *IEEE Journal of Solid-State Circuits*, 33(1), 109–118.
- Chen, K., Yang, Z., Hoang, L., Weiland, J., Humayun, M., & Liu, W. (2010). An integrated 256-channel epiretinal prosthesis. *IEEE Journal of Solid-State Circuits*, 45(9), 1946–1956.
- Li, X., Tsui, C.-Y., & Ki, W.-H. (2015). A 13.56 MHz wireless power transfer system with reconfigurable resonant regulating rectifier and wireless power control for implantable medical devices. *IEEE Journal of Solid-State Circuits*, 50(4), 978–989.
- Park, S. I., Brenner, D. S., Shin, G., Morgan, C. D., Copits, B. A., Chung, H. U., et al. (2015). Soft, stretchable, fully implantable miniaturized optoelectronic systems for wireless optogenetics. *Nature Biotechnology*, 33(12), 1280.
- Lee, J., & Nam, S. (2010). Fundamental aspects of near-field coupling small antennas for wireless power transfer. *IEEE Transactions on Antennas and Propagation*, 58(11), 3442–3449.
- Pan, J., Abidi, A. A., Rozgić, D., Chandrakumar, H., & Marković, D. (2017). 22.7 an inductively-coupled wireless power-transfer system that is immune to distance and load variations. In 2017 IEEE International Solid-State Circuits Conference (ISSCC). IEEE (pp. 382–383).
- Lee, B., Kiani, M., & Ghovanloo, M. (2016). A triple-loop inductive power transmission system for biomedical applications. *IEEE Transactions on Biomedical Circuits and Systems*, 10(1), 138–148.
- Huang, C., Kawajiri, T., & Ishikuro, H. (2018). A 13.56 MHz wireless power transfer system with enhanced load-transient response and efficiency by fully integrated wireless constant-idle-

- time control for biomedical implants. *IEEE Journal of Solid-State Circuits*, 53(2), 538–551.
- Tasneem, N.T., Biswas, D.K., & Mahbub, I. (2019). Closed-loop adaptive transcutaneous wireless power transfer system for implantable sensors. In 2019 IEEE radio and wireless symposium (RWS) (pp. 1–3).
- Xu, H., Bihr, U., Becker, J., & Ortmanns, M. (2013). A multichannel neural stimulator with resonance compensated inductive receiver and closed-loop smart power management. In 2013 IEEE international symposium on circuits and systems (ISCAS2013). IEEE (pp. 638–641).
- Wang, G., Liu, W., Sivaprakasam, M., & Kendir, G. A. (2005).
 Design and analysis of an adaptive transcutaneous power telemetry for biomedical implants. *IEEE Transactions on Circuits and Systems I: Regular Papers*, 52(10), 2109–2117.
- Wang, G., Liu, W., Bashirullah, R., Sivaprakasam, M., Kendir, G.A., Ji, Y., Humayun, M.S., & Weiland, J.D. (2004). A closed loop transcutaneous power transfer system for implantable devices with enhanced stability. In 2004 IEEE international symposium on circuits and systems (IEEE Cat. No. 04CH37512), IEEE (Vol. 4. pp. IV-17).
- Si, P., Hu, A. P., Malpas, S., & Budgett, D. (2008). A frequency control method for regulating wireless power to implantable devices. *IEEE Transactions on Biomedical Circuits and Systems*, 2(1), 22–29.
- Kiani, M., & Ghovanloo, M. (2010). An RFID-based closed-loop wireless power transmission system for biomedical applications. *IEEE Transactions on Circuits and Systems II: Express Briefs*, 57(4), 260–264.
- Kiani, M., Kwon, K.Y., Zhang, F., Oweiss, K., & Ghovanloo, M. (2011). Evaluation of a closed loop inductive power transmission system on an awake behaving animal subject. In 2011 annual international conference of the IEEE engineering in medicine and biology society. IEEE (pp. 7658–7661).
- Troyk, P. R., & Schwan, M. A. K. (1992). Closed-loop class E transcutaneous power and data link for micro-implants. *IEEE Transactions on Biomedical Engineering*, 39(6), 589–599.
- Hidayat, R., Rustam, R., Agustina, E., Wulandari, I.Y., & Rahim, R. (2018). A systematic approach to improving the performance of spiral antenna. INA-Rxiv. January (Vol. 13).
- Biswas, D. K., Tasneem, N. T., & Mahbub, I. (2019). Effects of coaxial-lateral and coaxial-angular displacements on link efficiency of a wirelessly powered optogenetic implant: design, modeling, and experimental validation. *IEEE Journal of Elec*tromagnetics, RF and Microwaves in Medicine and Biology, 3(4), 269–275.



- Raju, S., Wu, R., Chan, M., & Yue, C. P. (2014). Modeling of mutual coupling between planar inductors in wireless power applications. *IEEE Transactions on Power Electronics*, 29(1), 481–490.
- Biswas, D., Tasneem, N., Hyde, J., Sinclair, M., & Mahbub, I. (2018). Miniaturized wireless power transfer module design for brain optoelectronic implant. In 2018 IEEE international microwave biomedical conference (IMBioC). IEEE (pp. 163–165).
- 22. Tasneem, N.T., Suri, S.R., & Mahbub, I. (2018). A low-power CMOS voltage boosting rectifier for wireless power transfer applications. In 2018 Texas symposium on wireless and microwave circuits and systems (WMCS) (pp. 1–4).
- Saw, S.K., Meher, P., & Chakraborty, S.K. (2017). Design of high frequency d-flip-flop circuit for phase detector application. In TENCON 2017–2017 IEEE region 10 conference (pp. 229–233)
- Stan, M. R., Tenca, A. F., & Ercegovac, M. D. (1998). Long and fast up/downcounters. *IEEE Transactions on Computers*, 47(7), 722–735.

Publisher's Note Springer Nature remains neutral with regard to jurisdictional claims in published maps and institutional affiliations.



telemetry.



Nishat T. Tasneem (S'18) is a Ph.D. student and a Graduate Research Assistant in the Department of Electrical Engineering at the University of North Texas. She has received the B.Sc. degree in Electrical and Electronic Engineering from Bangladesh University of Engineering and Technology in 2016. Her research interests include low-power IC design for implantable and wearable sensors, wireless power transfer system design and wireless data

Dipon K. Biswas (S'18) is a Ph.D. student and a Graduate Research Assistant in the Department of electrical engineering at the University of North Texas. He has completed his B.S. in electrical engineering from Khulna University of Engineering and Technology (KUET), Bangladesh in May 2016. He is currently working on antenna design and optimization for wireless power transfer applications. research interest includes

microwave system and antenna design, wireless power transfer system, analog and RF circuit design.



Ifana Mahbub (S'12-M'17) is an Assistant Professor in the Department of Electrical Engineering at the University of North Texas, where she is the director of the Integrated Biomedical Circuits and Systems Laboratory (iBioCASL). Her research interests include energy efficient circuits and systems design for wireless data telemetry, power transfer and signal processing applications for implantable and wearable sensors. Her works also focus

on the RF and microwave component designs and miniaturized, flexible antenna design. She received the B.Sc. degree (2012) in Electrical and Electronic Engineering from Bangladesh University of Engineering and Technology, Bangladesh and the Ph.D. degree (2017) in Electrical Engineering and Computer Science from the University of Tennessee, Knoxville. She received the "Early Career Award" from the National Science Foundation in 2020. Dr. Mahbub has published 2 book chapters, 16 journal publications, and over 31 peer-reviewed conference publications. She is the Vice-chair of the IEEE Circuits & Systems Society, Dallas Chapter. She is serving as a guest editor for the MDPI Journal of Low-Power Electronics and Applications, publications chair for the 2018, 2019 and 2020 IEEE MTT Texas Symposium on Wireless & Microwave Circuits & Systems (TSWMCS) conferences, 2018 Dallas Circuits and System (DCAS) conference and student paper competition chair for the 2018 IEEE MTT-S International Microwave Biomedical Conference (IMBioC).

